

www.acsami.org Research Article

# Nano-optoelectrodes Integrated with Flexible Multifunctional Fiber Probes by High-Throughput Scalable Fabrication

Shan Jiang, <sup>∇</sup> Junyeob Song, <sup>∇</sup> Yujing Zhang, <sup>∇</sup> Meitong Nie, <sup>∇</sup> Jongwoon Kim, Ana Lopez Marcano, Kelly Kadlec, William A. Mills, III, Xiaodong Yan, Hefei Liu, Rong Tong, Han Wang, Ian F. Kimbrough, Harald Sontheimer, Wei Zhou, \* and Xiaoting Jia\*



Cite This: ACS Appl. Mater. Interfaces 2021, 13, 9156-9165



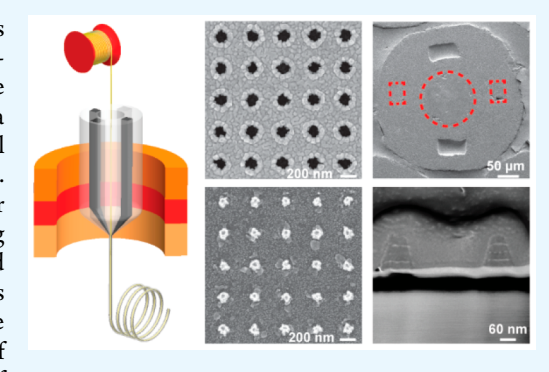
**ACCESS** 

Metrics & More



s Supporting Information

ABSTRACT: Metallic nano-optoelectrode arrays can simultaneously serve as nanoelectrodes to increase the electrochemical surface-to-volume ratio for high-performance electrical recording and optical nanoantennas to achieve nanoscale light concentrations for ultrasensitive optical sensing. However, it remains a challenge to integrate nano-optoelectrodes with a miniaturized multifunctional probing system for combined electrical recording and optical biosensing in vivo. Here, we report that flexible nano-optoelectrode-integrated multifunctional fiber probes can have hybrid optical—electrical sensing multimodalities, including optical refractive index sensing, surface-enhanced Raman spectroscopy, and electrophysiological recording. By physical vapor deposition of thin metal films through free-standing masks of nanohole arrays, we exploit a scalable nanofabrication process to create nano-optoelectrode arrays on the tips of flexible multifunctional fiber probes. We envision that the development of



flexible nano-optoelectrode-integrated multifunctional fiber probes can open significant opportunities by allowing for multimodal monitoring of brain activities with combined capabilities for simultaneous electrical neural recording and optical biochemical sensing at the single-cell level.

KEYWORDS: multifunctional fiber-based neural probe, convergence fiber drawing, nano-optoelectrodes, nanoplasmonic sensing, in vivo neural recording

# INTRODUCTION

By supporting surface plasmon modes to concentrate optical fields at the nanoscale, plasmonic metal nanostructures can serve as optical nanoantennas to achieve ultrasensitive spectroscopic bio/chemical sensing. In particular, the refractive index (RI) plasmonic sensors can monitor surface-binding events of biomarker molecules by resolving RI-dependent spectral shifting of surface plasmon resonances; 1-3 surfaceenhanced Raman spectroscopy (SERS) plasmonic sensors can provide vibrational fingerprint spectra of analyte molecules by enhancing both excitation and inelastic scattering processes in hot spots. 4-6 In the attempts of creating plasmonic metal nanostructures on the tips of optical fibers for in situ remote optical biosensing,  $^7$  a new technology called "Lab on Fiber" has been developed.  $^{8-12}$  Most of these previous works have used bottom-up or top-down nanofabrication methods such as selfassembly surface functionalization, electron-beam lithography, and focused-ion-beam patterning to integrate the plasmonic metal nanostructures with optical fibers.7,13-17 These approaches, however, have challenges for simultaneous achievement of good accuracy, throughput, and scalability in manufacturing nanoantenna-integrated fiber systems, which limits their potential in real-world applications. Furthermore, plasmonic nanoantennas consisting of high-conductivity noble metal nanostructures can also function as nanoelectrodes with a large electrochemical surface-to-volume ratio for high-performance electrical recording, <sup>18</sup> and thus can essentially serve as nano-optoelectrodes for hybrid optical-electrical sensing in biochemical systems.

For in vivo electrical biosensing, fabricating silicon-based microelectrode arrays by a top-down semiconductor fabrication process has become a robust and scalable technology to enable multichannel monitoring of neural activities in the brain, <sup>19–22</sup> which, however, faces difficulties in long-term in vivo operation due to the mismatch of the biomechanical properties between the soft brain tissue and the rigid devices. Furthermore, most of the silicon-based devices are limited to a single functionality. Recently, flexible multimaterial, multifunc-

Received: October 26, 2020 Accepted: February 2, 2021 Published: February 10, 2021





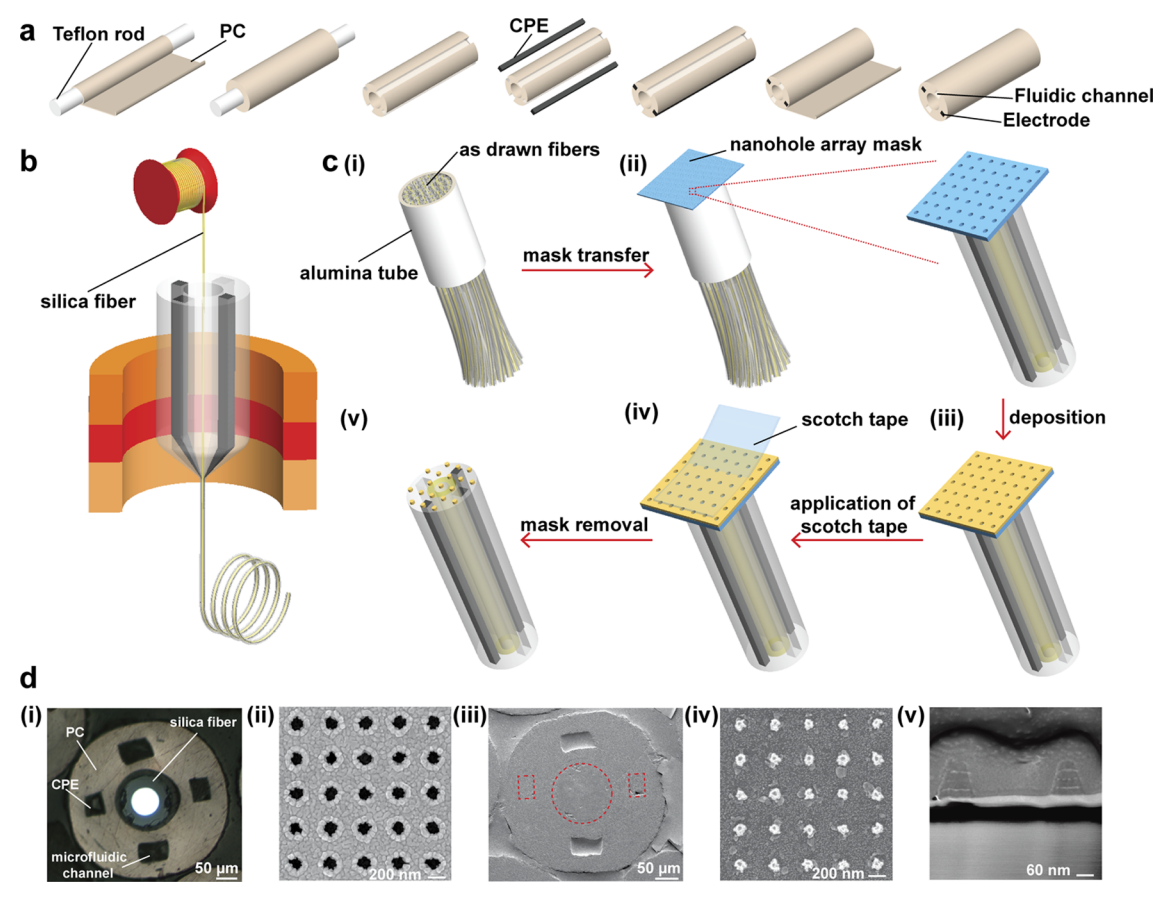


Figure 1. Fabrication of nano-optoelectrodes on multifunctional fiber tips. (a) Schematic showing the fabrication process of the preform with two electrodes, two fluidic channels, and a hollow core. (b) Illustration of the fiber drawing process. The silica fiber was inserted into the center hole and converged with the polymer material during the thermal drawing process. (c) Schematic illustration of the process of integrating the nano-optoelectrodes on the fiber tips: (i) As-drawn fibers were cut, bundled, and inserted into an alumina tube. (ii) After the fixation and polishing process, a nanohole array mask was transferred to the top surface of the bundle. (iii) Following the mask transfer, layers of Ti, Au, and Ag were deposited onto the polymer fiber bundle tip via e-beam evaporation. (iv) The nanohole array mask was peeled off using Scotch tape, leaving behind the periodic nanostructures as shown in (v). (d) Optical and SEM images of the multifunctional fiber, nanohole array mask, and nano-optoelectrodes: (i) optical image of the as-drawn multifunctional fiber in the bundle after polishing; (ii) SEM image of the nanohole array mask; (iii) SEM image of the fiber tip with periodic nano-optoelectrodes deposited; (iv) zoomed-in SEM image showing the nano-optoelectrodes on the silica fiber; and (v) cross-sectional SEM image of the nano-optoelectrodes.

tional fiber probes have proved their superiority not only in the outstanding biomechanical compatibility to allow chronic in vivo electrical recording at a single-cell level but also in bidirectional in vivo communication capability for both optical and electrical biosignals. Therefore, multimaterial, multifunctional fiber probes can be used as a combined optical–electrical transmission line platform to integrate with nano-optoelectrodes at the fiber probe tip for hybrid optical–electrical biointerfacing at a single-cell level in vivo.

In this work, we demonstrate the integration of dense nano-optoelectrode arrays on the tips of multifunctional optoelectrical fibers by high-throughput scalable fabrication. The multifunctional fibers are fabricated using a convergence fiber drawing technique that allows for polymer electrodes and silica waveguides to be codrawn into a flexible micron-sized fiber device. The dense arrays of nano-optoelectrodes composed of Au/Ag nanolaminated nanodisks are created on the tips of flexible multifunctional probes by electron beam deposition of alternating metal layers through free-standing nanohole array masks. This unique surface modification enables us to detect chemicals through the fiber tip via RI optical sensing and SERS molecular detection, which holds great potential to sense

biomarkers in vivo. Beyond optical sensing, we demonstrate that the nano-optoelectrodes can improve the electrical recording performance of the polymer composite electrodes by reducing the impedance of the electrodes. Moreover, we were able to record neural activity from the hippocampus region of mouse brains 28 weeks postimplantation, demonstrating good biocompatibility of these integrated probes for potential chronic implant applications.

# ■ RESULTS AND DISCUSSION

Fabrication of Nano-optoelectrodes on Multifunctional Fibers. In previously reported studies, <sup>23–25</sup> Canales and co-workers developed multifunctional fiber-based neural interfaces using a polymer waveguide and surrounding polymer electrodes. However, the large transmission loss in this kind of polymer waveguide makes it unsuitable for ultrasensitive optical sensing. To address this issue, we drew a multifunctional polymer fiber with a silica fiber in the center. Two conductive polymer electrodes (conductive polyethylene, CPE) were incorporated into a macroscopic preform via a machining process while the center of the preform remained hollow (Figure 1a). We then inserted the silica fiber with a

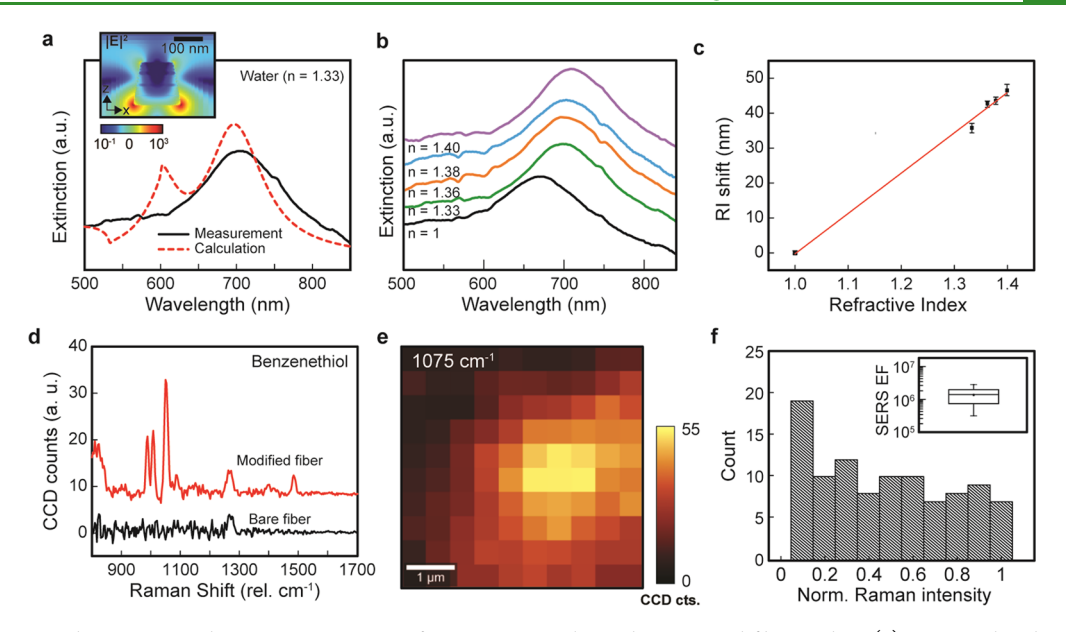


Figure 2. Refractive index sensing and SERS measurements from nano-optoelectrode-integrated fiber probes. (a) Measured and FDTD-calculated extinction spectra of nano-optoelectrode arrays on the fiber probes in the water showing a distinct peak of localized surface plasmon mode. (Inset) FDTD-calculated x-z distribution map (697 nm). (b) Measured extinction spectra of nano-optoelectrode-integrated fiber probes with different background refractive index environments, including air (n = 1), water (n = 1.33), ethanol (n = 1.36), IPA (n = 1.38), and butanol (n = 1.40). (c) Dependence of the wavelength shifts of the resonant extinction peak on the refractive index changing from 1 to 1.40. (d) Measured average SERS spectra of BZT for fiber probes with and without the surface modification of nano-optoelectrode arrays. (e) 2D Raman image of a 5  $\mu$ m × 5  $\mu$ m area for the BZT Raman peak at 1075 cm<sup>-1</sup>. (f) Histograms of SERS intensities on the surface of nano-optoelectrode-integrated fiber probes. (Inset) Calculated SERS EFs.

polyimide coating into the center orifice, which was then pulled down to converge with the surrounding polymer during the thermal drawing process shown in Figure 1b.26,27 The optical property of the silica fiber was not altered during the fiber drawing process based on the transmission spectrum measurement before and after drawing (Figure S1). The drawn fibers were cut, bundled, and inserted into an alumina tube and fixed using phenyl salicylate (Figure 1c(i)). After the fixation, the bundle was polished on lapping films, resulting in submicron roughness for deposition in the next step. Following the transfer of the nanohole array mask (nanohole diameter = 130 nm, periodicity = 400 nm) onto the tip surface of the polymer fiber bundle (Figure 1c(ii)), we used electron-beam evaporation to deposit a 1 nm thick Ti adhesion layer and alternating Au and Ag layers (thickness = 25, 6, 25, 8, and 25 nm from bottom to top) as shown in Figure 1c(iii). 28,29 Next, Scotch tape was used to remove the nanohole array mask (Figure 1c(iv)), leaving the periodic nano-optoelectrodes on the tip of the fibers (Figure 1c(v)). The use of the Au nanohole array mask can result in a high-yield and reproducible fabrication process of nano-optoelectrodes, compared to other nanofabrication techniques, such as ebeam lithography. As described in our previous work, 28,29 the Au nanohole array mask is fabricated on a 3-in. wafer and can be cut into pieces depending on the substrate size in use. After the nanohole array mask transfer process, only one e-beam evaporation and lift-off process is needed to integrate the plasmonic nano-optoelectrodes with the multifunctional fibers. The structure of the nano-optoelectrodes has been optimized based on our previous work.<sup>30</sup>

Figure 1d(i) shows a cross-sectional optical image of an asdrawn fiber in the bundle after polishing. To investigate the structure of the nanohole array mask and nano-optoelectrodes on the fiber tips, we used a scanning electron microscope

(SEM) to characterize the nanostructures of the mask as shown in Figure 1d(ii). Figure 1d(iii) shows the SEM image of the as-drawn multifunctional fiber with nano-optoelectrodes deposited, and Figure 1d(iv) presents a zoomed-in SEM image of nano-optoelectrodes on the silica fiber tip surface. To further validate the layers of the nano-optoelectrode, the focused ion beam (FIB) technique was utilized, and the corresponding cross-sectional SEM image of the nano-optoelectrodes is shown in Figure 1d(v).

Refractive Index Sensing and SERS Measurement. To examine the optical properties of nano-optoelectrode arrays on fiber, we conducted optical extinction measurements through the fiber tip surface at the normal-incident angle. As shown in Figure 2a (solid line), the extinction spectrum shows a major peak at ~705 nm for the localized surface plasmon resonance in nanolaminated Au-Ag-Au nano-optoelectrode arrays. The calculated extinction spectrum by 3D finite-difference timedomain (FDTD) methods also reveals a distinct resonant peak at 697 nm (dashed line in Figure 2a), in good agreement with the measurements. The FDTD-calculated  $|E|^2$  distribution map (Figure 2a (inset)) reveals that the localized surface plasmon mode has an electric dipole nature with intense optical fields, mostly concentrated at the bottom edges of individual nanooptoelectrodes. Compared to the calculation, the resonant feature in the measurements shows a broader line width due to the inhomogeneous broadening effects from size variations between individual nanoantennas in the array.<sup>30</sup>

As a proof-of-concept demonstration for plasmonic RI sensing, we used nano-optoelectrode-integrated fiber probes to monitor the resonant shifts of plasmonic dipole mode in response to the RI changes in the background environment. The RI-sensing measurements are conducted after acetone—IPA rinse cycles, demonstrating good stability of the nanostructures. Figure 2b depicts the measured extinction

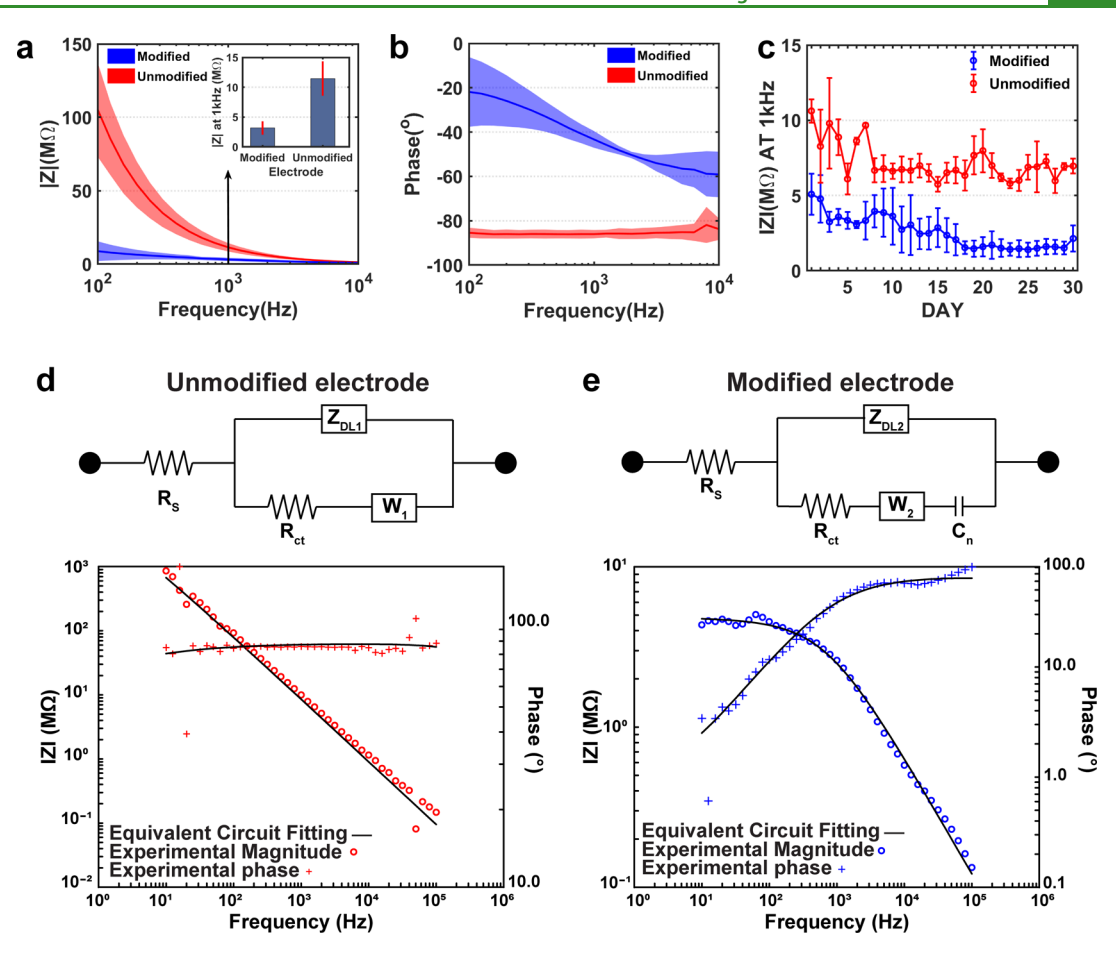


Figure 3. Electrochemical impedance spectroscopy (EIS) measurements and the equivalent circuit model fitting of the electrode before and after surface modification. (a) Bode magnitude impedance plot of the CNF-CPE electrode showing the lower impedance characteristics of the electrode after surface modification. (b) Bode phase impedance plot of the CNF-CPE electrodes indicating the less capacitive behavior of the electrode with the interrogation of nano-optoelectrodes. (c) CNF-CPE electrode with and without surface modification soaked in 1× PBS for 30 days with the impedance recorded daily. We can observe that the impedance of the surface-modified electrode is relatively stable, with a slight decrease in the magnitude of the impedance at 1 kHz, while the unmodified electrode exhibits similar behaviors. (d) Equivalent circuit model (modified Randles circuit) of the unmodified electrode and the representative EIS impedance spectra for experimental data (red) and equivalent circuit fitting (black) used for curve fitting. It is composed of electrolyte resistance ( $R_{\rm s}$ ) in series with a parallel combination of the double-layer capacitor ( $Z_{\rm DL}$ ), Warburg impedance ( $W_{\rm 1}$ ), and charge-transfer resistance ( $R_{\rm ctl}$ ). (e) Equivalent circuit model of the modified electrode and the representative EIS impedance spectra for experimental data (blue) and equivalent circuit fitting (black) used for curve fitting. A pseudocapacitor ( $C_{\rm n}$ ) was introduced to the circuit and in series of the Warburg impedance to represent the redox energy stored at the surfaces of nano-optoelectrodes.

spectra for the optoelectrode-integrated fiber probes, respectively, in air (n=1), water (n=1.33), ethanol (n=1.36), isopropyl alcohol (IPA, n=1.38), and butanol (n=1.40). As the RI of the surrounding medium increases, the plasmonic resonant peak red-shifts from 667 nm (n=1) to 703 nm (n=1.33), 710 nm (n=1.36), 711 nm (n=1.38), and 714 nm (n=1.4), respectively. By a linear regression fitting of the measured dependence between RIs and the relative spectral shifts of the resonant peaks, we can obtain an RI sensitivity of  $\sim$ 115.54 nm/RIU for the plasmonic nanodisk arrays (Figure 2c). The FDTD-simulated extinction spectra (Figure S2) in different background refractive index environments agree well with the measurements.

By measuring Raman spectra of benzenethiol (BZT) molecules functionalized on the surface of nano-optoelectrodes, we have examined the SERS performance of nano-optoelectrode-integrated fiber probes. As shown in Figure 2d, nano-optoelectrode-integrated fiber probes can induce intense BZT Raman signals featured by four notable BZT vibrational peaks at 1004 cm<sup>-1</sup> (the CCC ring in-plane bending mode),

1026 cm<sup>-1</sup> (the CH in-plane bending mode), 1075 cm<sup>-1</sup> (the CCC ring in-plane breathing mode with CS stretching mode), and 1578 cm<sup>-1</sup> (the CC stretching mode). In contrast, the bare fiber probes without plasmonic nanostructures do not exhibit these characteristic BZT Raman peaks due to the lack of local optical field enhancement. Figure 2e shows the 2D confocal Raman images (at 1075 cm<sup>-1</sup>) over a 5  $\mu$ m × 5  $\mu$ m area. For the analysis of SERS performance on nano-optoelectrodes at the fiber probe tip, we plotted the histograms of 1075 cm<sup>-1</sup> Raman signal intensities from 10 × 10 pixels and found an average SERS enhancement factor (EF) of ~1.4 × 10<sup>6</sup> for the samples (Figure 2f). The SERS EFs were calculated by the following formula, <sup>31</sup>

$$EF = (I_{SERS}/I_{Raman}) \times (N_{Raman}/N_{SERS})$$
 (1)

where  $I_{\rm SERS}$ ,  $I_{\rm Raman}$ ,  $N_{\rm Raman}$ , and  $N_{\rm SERS}$  are SERS BZT intensity, neat BZT Raman intensity, and the number of BZT molecules contributing to SERS and neat Raman intensities, respectively.

Electrical Characterization of the Surface-Modified Electrodes. To evaluate the effect of nano-optoelectrodes on

	$R_{\rm s}~({\rm K}\Omega)$	$Y_{01} (S \times S^{A1})$	A1	W1 $(S \times S^{1/2})$	$R_{\rm ct1}~({ m M}\Omega)$
mean	4.356	$21.65 \times 10^{-12}$	0.956	$34.71 \times 10^{-12}$	2.14
SD	0.051	$1.34 \times 10^{-12}$	0.024	$4.11 \times 10^{-12}$	0.34

Table 1. Means and Standard Deviations (SD) of Parameters in the Equivalent Circuit Model with the Unmodified Probe

the fiber electrodes, we compared the electrical performance of the fibers with surface-modified and unmodified electrodes. In our previous study, we proved that the impedance of the carbon nanofiber composite electrode (CNF-CPE) was significantly decreased compared with the conventional CPE electrode due to the alignment of the CNFs.<sup>24</sup> However, the impedance is still relatively high compared to other commonly used neural recording electrodes. Here, we deposited nanooptoelectrodes onto CNF-CPE electrodes using e-beam evaporation of Ti/Au/Ag/Au/Ag/Au with thicknesses of 1/ 25/6/25/8/25 nm by using the method shown in Figure 1 and measured the impedance spectra of the electrode. Parts a and b of Figure 3 show the Bode plot of the impedance spectra acquired from a potentiostat using a three-electrode measurement method with the fiber electrode as the working electrode, a Pt wire as the counter electrode, and Ag/AgCl as the reference electrode. From the Bode magnitude impedance plot (Figure 3a), we can observe an evident decrease in impedance for surface-modified electrodes at 1 kHz, a frequency where the action potential's firing frequency band was centered.<sup>32</sup> The Bode phase plot (Figure 3b) also suggests that, after surface modification, the electrode exhibits a less capacitive behavior, while the unmodified electrode manifests a capacitor-dominant behavior over the whole frequency range. For evaluating the performance of the surface-modified electrodes as a long-term neural implant device, the electrodes were soaked in 1× PBS solution for 30 days, and the impedance spectra were recorded daily. Figure 3c shows that the impedance of the surfacemodified electrode at 1 kHz is relatively stable, with a slight decrease over time. This may result from the slightly porous structure of the electrode material as the unmodified electrode demonstrates the same decrease of impedance at 1 kHz.

To further understand how the deposited nano-optoelectrodes improve the electrical performance of the CNF-CPE electrodes, we first curve-fitted the experimental EIS data of unmodified electrodes to a modified Randles circuit,  $^{18,33-35}$  as shown in Figure 3d. This model contains a solution resistance,  $R_s$ , in series with a parallel combination of a constant phase element representing a double-layer capacitor ( $Z_{\rm DL1}$ ), a charge-transfer resistance ( $R_{\rm ct1}$ ), simulating Faradaic reactions, and a Warburg impedance presenting the diffusion process. The constant phase element (a capacitor with nonideal capacitor behavior) is defined as

$$Z = 1/Y_0(jw)^n \tag{2}$$

where  $Y_0$  is the capacitance of the constant phase element and n is the phase factor (for an ideal capacitor, n=1). <sup>18,36</sup> The parameters for this equivalent circuit model are listed in Table 1 with mean values and standard deviations. For the surface-modified electrodes, we introduced a pseudocapacitor to be in series with the Warburg element to represent the redox energy stored at the nanostructured surfaces of nano-optoelectrodes arrays, <sup>37,38</sup> while all the other elements remain unchanged, and the curve-fitted results are shown in Figure 3e. Then we applied the fitted solution resistance result from Table 1 to the experimental EIS data of surface-modified electrodes, and the curve-fitted parameters are shown in Table 2.

Table 2. Means and Standard Deviations of Parameters in the Equivalent Circuit Model with the Surface-Modified Probe

	$Y_{02} \ (S \times S^{A2})$	A2	$W_1$ $(S \times S^{1/2})$	$R_{\rm ct1}~({ m M}\Omega)$	$C_{\rm n}~(\mu {\rm F})$
mean	$383 \times 10^{-12}$	0.749	$2.3 \times 10^{-6}$	4.91	1.47
SD	$18.3 \times 10^{-12}$	0.04	$0.58 \times 10^{-6}$	0.27	0.44

By comparing the parameters from these two tables, we can conclude that the deposited nano-optoelectrodes have increased the double-layer capacitance and promoted the charg-transfer reaction between the electrode surface and the electrolyte, resulting in a decrease of the impedance value. Also, the decrease in the phase factor further validates the increase of the surface roughness, <sup>39,40</sup> as well as the lower capacitive behavior of the electrode after nano-optoelectrodes deposition.

In Vivo Electrophysiology. To evaluate the recording capability of the surface-modified electrodes, we implanted the fibers into the hippocampus region of five wild-type mice for an in vivo electrophysiology study. Figure 4a shows a photograph of a healthy mouse with a small probe implanted for 24 days. Twenty-four days after the implantation, we started recording, and a representative trace of the raw recordings from the hippocampus region of the mice is shown in Figure 4b. The recorded signal was bandpass-filtered from 0.3 to 300 Hz and 300 to 5000 Hz to isolate the local field potential (LFP) and single-unit activities, respectively. From the bandpass-filtered spiking activities, two representative spike clusters were distinctively isolated among many other spike clusters via principal component analysis (PCA) and K-means clustering. The two clusters can be observed in the recording data, in the action potentials, and in the PCA with the corresponding matching colors, which demonstrates our surface-modified electrodes' recording capability with a single-unit resolution (Figure 4c). We also calculated the two standard metrics, L-ratio and isolation distance, to evaluate the separations of spike clusters. From the 1-min-long recording, the L-ratio and the isolation distance (ID) of the two clusters were 0.024 and 18.28, respectively.

We repeated recordings of neural activities 28 weeks after implantation in five animals, as shown in Figure 4d and e. A representative 2.5-s electrophysiology recording is shown in Figure 4d. The top trace shows the unfiltered signal, the middle trace represents the LFP recording, and the bottom one shows the spiking activities. Two isolated clusters were sorted from the recorded signal via the PCA analysis (Figure 4e). The L-ratio and the ID of two isolated clusters were 0.07 and 40.97, respectively. Clusters with an L-ratio lower than 0.2 and an ID larger than 20 are considered well-separated single neurons. Thus, the surface-modified electrodes presented reliable and stable recording performance over an extended period of chronic implantation.

To compare the recording performance of the CNF-CPE electrode before and after surface modification with nano-optoelectrodes, we implanted surface-modified and unmodified polymer electrodes to the hippocampal formation of three

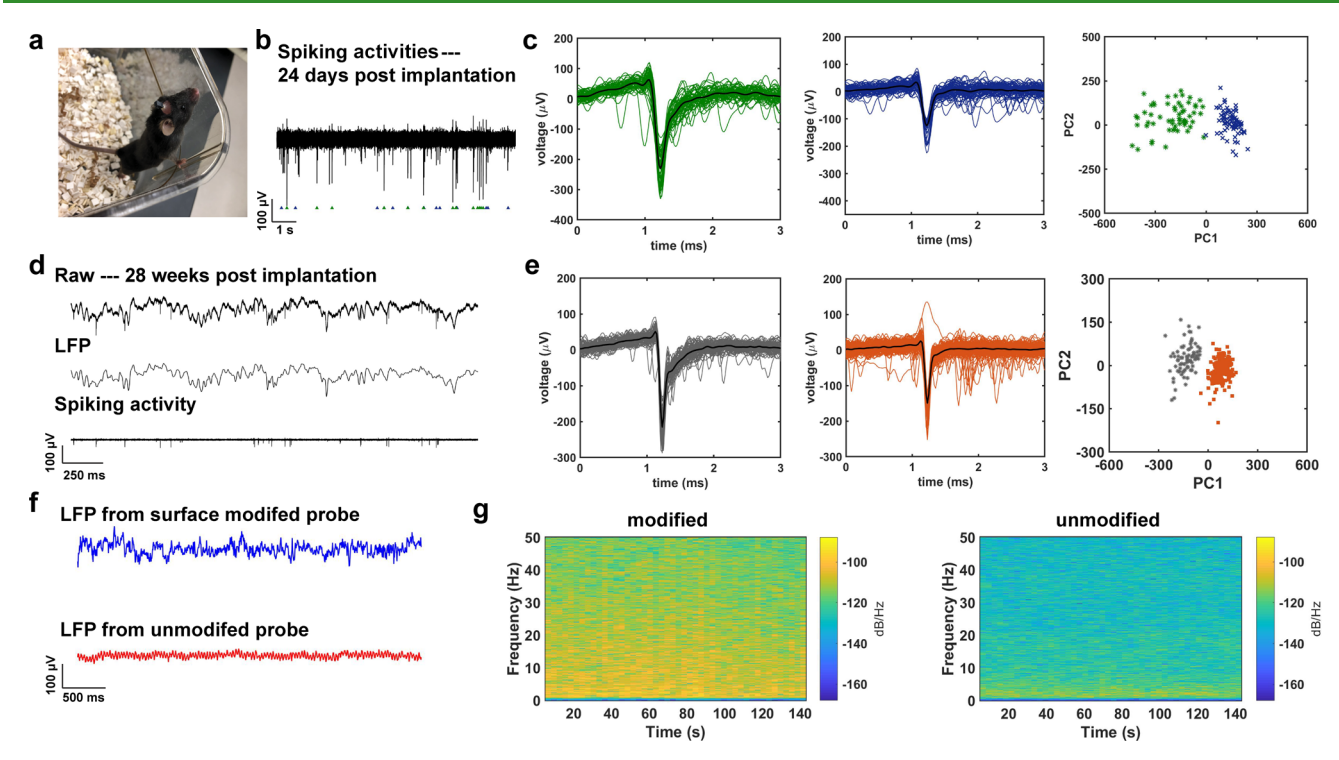


Figure 4. Electrophysiology recording from the surface-modified CNF-CPE electrodes and its comparison with that from the unmodified electrodes. (a) Photograph of a mouse with the small CNF-CPE electrode implanted for 24 days. (b) Representative trace of spiking activities acquired from the surface-modified electrode 24 days postimplantation. (c) Two distinct clusters isolated from the recorded signal via PCA. (d) Representative recorded electrophysiological signal following 28 weeks of implantation. The top trace shows the unfiltered signal, the middle trace shows the bandpass-filtered (0.3–300 Hz) LFP, and the bottom trace represents the bandpass-filtered (0.5–5 kHz) spiking activity. (e) Two clustered units sorted from the recording result and the corresponding PCA, indicating the quality of these two clusters. (f) CNF-CPE electrodes with and without nano-optoelectrodes on day 0 recorded for 2.5 s of LFPs, showing a better recording performance with the surface-modified electrode. (g) Spectrograms of a 140-s-long LFP trace from both surface-modified and unmodified electrodes. We observed relatively higher powers in each frequency bin from the CNF-CPE electrode with nano-optoelectrodes.

wild-type mice and conducted power spectral analysis on the LFP recordings obtained from these electrodes. Figure 4f shows representative 2-s traces of LFP recording results from the CNF-CPE electrode with and without surface modification. One can observe that the peak-to-peak amplitude of the LFP trace acquired from the modified electrode was, on average, higher in magnitude than that acquired from the unmodified electrode. The frequency ranges of the content of the signal we investigated are, namely, delta (0.5-3 Hz), theta (4-7 Hz), alpha (8-13 Hz), and beta (14-40 Hz) waves. As expected, in the spectrograms of a 140-s-long LFP trace from both electrodes, we observed relatively higher powers in each frequency bin with the surface-modified electrodes (Figure 4g). The resulting plot of the multitaper power spectral density estimate (Figure S3) also confirmed a systematically higher power density with nano-optoelectrodes modification.

Biocompatibility of the Surface-Modified Electrode. The reactive tissue response to our surface-modified neural probe was assessed using immunohistochemical analysis of surrounding brain tissue from mice implanted for 2 weeks with either a surface-modified probe or a conventional stainless steel probe. The presence of glial fibrillary acidic protein (GFAP) was used to assess astrocyte reactivity to the probe, ionized calcium-binding adaptor molecule 1 (Iba1) was used as a marker of microglial response, and the neuron-specific protein NeuN was used to analyze neuronal density. Representative images from the contralateral side of an implanted brain (control), a surface-modified probe, and a stainless steel probe

are presented in Figure S4. Neuronal density, microglia density, and astrocyte reactivity were compared between all groups, and no significant difference was observed (Figure S4e-g).

### CONCLUSION

We have developed a scalable method for fabricating nanooptoelectrode arrays on tips of multifunctional fibers by using free-standing nanohole array deposition masks. The integration of nanolaminated nanoantenna arrays allows us to conduct RI optical sensing and surface-enhanced Raman spectroscopy on the fiber tip. In the meantime, the conductive metal nanostructures can enhance the electrical recording performance of the polymer-based microelectrodes, demonstrating a larger power density of local field potential (LFP) compared with unmodified probes. These nano-optoelectrode-integrated probes were able to provide continuous electrophysiology measurements up to 28 weeks postimplantation, indicating good biocompatibility of these probes, consistent with our immunohistochemistry analysis. All these results indicate that we have developed a miniaturized multifunctional neural probe platform that can integrate optical nanoplasmonic biosensors and neural recording microelectrodes on the tip of a flexible and biocompatible polymer fiber. This work will pave the way toward new multimodal detection approaches for a deeper understanding of brain function in both electrophysiological and biomolecular aspects.

#### **■ EXPERIMENTAL METHODS**

Thermal Fiber Drawing Process. A preform was prepared to draw the multifunctional fiber with silica fiber inside. First, polycarbonate (PC) films (Laminated Plastics) were wrapped around a polytetrafluoroethylene (PTFE) rod (U.S. Plastic Corp.) and consolidated to a PC tube with thick walls. Then four grooves were machined on the PC tube, and two of the grooves were inserted with commercially available conducting polyethylene (CPE, Hillas Packaging) as the electrodes, while the other two remained hollow as the microfluidic channels. After the insertion of electrodes, additional PC films were wrapped around the structure and consolidated to a macroscopic template. Before the thermal drawing process, the silica fiber (AFH105/125/145T, Fiberguide) was inserted into the hole in the preform center and was fixed to the preform bottom, which enabled the flow of silica fiber as being pulled during the polymer thermal drawing process. Also, a multifunctional fiber made of PVDF (polyvinylidene difluoride) was fabricated using the same method with an additional PC layer as a sacrificial layer to support a stable

**Bundle Process.** To maximize the usage of the Au nanohole arrays mask, the outer sacrificial PC layer was etched away by immersion in dichloromethane for 2–4 min for each fiber with reasonable impedance data. Then fibers were inserted into a piece of nonporous alumina ceramic tube (McMaster-Carr) and fixed by phenyl salicylate on both ends. After the fixation, a similar size hole was created in the center of a PC rod, and the ceramic tube was fixed inside this hole using the same method described above. To obtain a flat surface for the future deposition process, the fiber bundle was polished by optical polishing papers (30, 12, 5, 1, and 0.5  $\mu$ m, Fiber Optic Center), resulting in submicrometer roughness.

Nanolaminated Plasmonic Nanoantenna Deposition. Before the deposition, the fiber bundle was polished by oxygen plasma. The Au nanohole array mask was prefabricated on a Si substrate with a 10nm thick Cr sacrificial under the Au layer. Cr etchant (Chromium Etchant 1020, Transene, U.S.A.) was used to lift off this Au nanohole array mask.<sup>21</sup> The thickness of the nanohole array mask is ~150 nm, with a nanohole array diameter of ~130 nm and a periodicity of 400 nm. After etching the Cr layer, we introduced deionized water between the Au nanohole array and the silicon substrate to float it up. Then we scooped the mask onto an oxygen plasma-treated glass substrate and transferred it onto the fiber bundle surface with drying overnight at room temperature. Before depositing the alternating Au-Ag layers, a thin layer of Ti of 1 nm was deposited onto the bundle substrate through the nanohole array as an adhesion layer, and then alternating layers of Au and Ag were deposited with layer thicknesses of 25, 6, 25, 8, and 25 nm from bottom to top for the CNF fiber, while the thicknesses were 25, 6, 25, 8, 25, 10, and 25 nm for the multifunctional fiber. Finally, the nanohole array mask was peeled off by Scotch tape, leaving the periodic nanoantenna arrays on the bundle surface. After the deposition, the ceramic tube was removed from the PC rod by applying heat through the hot gun, and the same process was repeated to separate fibers from the ceramic tube. Following the separation, the fiber was cleaned by dichloromethane to remove phenyl salicylate residue and rinsed by isopropyl alcohol (MilliporeSigma) for further cleaning.

Raman Measurement. BZT (Sigma-Aldrich, U.S.A.) was used as the probe molecules to evaluate the SERS performance of the modified fiber. The fiber tip was incubated in  $1 \times 10^{-3}$  M of BZT ethanolic solution for 24 h to form a self-assembled monolayer. A confocal Raman microscope (Alpha 300 RSA+, WITec, Germany) equipped with a 785 nm diode laser (Toptica Photonics, Germany) was used for the SERS measurements. BZT signals were collected via  $20\times$  objective (NA = 0.4) with 3 mW and 0.1 s integration time. Before the measurement, the instrumental calibration was verified using a silicon wafer by the silicon peak at 520 cm<sup>-1</sup>. The back-scattered photons were detected by a spectrometer (UHTS300, WITec, Germany) equipped with a CCD camera (DU401A, Oxford Instruments, U.K.). Cosmic ray removal and baseline correction were

conducted by instrument-embedded software (Project v4.1, WITec, Germany) after the signal acquisition.

**Refractive Index Measurement.** A halogen light source (DH 2000, Ocean Optics, U.S.A.) was utilized to illuminate the nano-optoelectrode-modified fiber tip via  $20\times$  objective (NA = 0.4) using the microscope configuration of an existing microscope (Alpha300 RSA+, WITec, Germany) schematically shown in Figure S5. The transmitted light under normal excitation was collected at the end of the fiber sensor with a fiber-coupled spectrometer (Flame, Ocean Optics, U.S.A.). For examining the sensitivity of the nano-optoelectrodes deposited onto the fiber tip to changes in refractive indices, optical transmission spectra were measured as the sensor tip was immersed in different liquid solutions such as water (n = 1.33), ethanol (n = 1.36), isopropyl alcohol (n = 1.38), and butanol (n = 1.4). The transmission spectra are normalized by reference spectra measured using an unmodified fiber and noise. The normalized transmission spectra were calculated by the following,

$$I_{\text{normalized}} = (I_{\text{sample}} - I_{\text{noise}}) / (I_{\text{reference}} - I_{\text{noise}})$$
(3)

where  $I_{\text{sample}}$ ,  $I_{\text{noise}}$ , and  $I_{\text{reference}}$  are the transmission spectra of the modified fiber and the noise and transmission spectra of the unmodified fiber, respectively.

Electrochemical Impedance Spectrum. Two-cm-long fiber sections of surface-modified and unmodified fibers with similar crosssectional sizes (25.7  $\mu$ m × 16.6  $\mu$ m) were prepared and connected with a copper wire via silver paint. A potentiostat (Interface 1000E, Gamry Instruments) was utilized to obtain the impedance measurement results with 1× phosphate-buffered saline (PBS, Thermo Fisher) as the electrolyte. To evaluate the change in impedance results before and after surface modification of the polymer electrode, we performed a three-electrode experiment with polymer fiber, Ag/AgCl electrode (Cole-Pamer), and a Pt wire (Basi), which serve as the working electrode, reference electrode, and counter electrode, respectively. An ac voltage of 10 mV with a frequency ranging from 10 Hz to 100 kHz was applied, and the impedance measurement results were recorded accordingly. To discover the impact of silver oxidation on electrode electrical characteristics, the polymer fiber tip was soaked in 1× PBS, and two-electrode EIS experiments, which mimic the two-electrode recording environment in a mouse brain, were conducted daily for 2 weeks. The exciting ac voltage remained the same, while the frequency range changed to 100 Hz to 10 kHz.

**Neural Probes Assembly.** Conductive silver paint was applied on the fiber tip to connect the copper wire, which was soldered to headpins (Sullins Connector Solutions), while the ground wire was a soldered stainless steel wire (GoodFellow). Then 5-min epoxy (Devcon) was used to fix these wires as well as insulate the exposed electrical conducting parts.

Surgical Procedures. All animal procedures were approved by the Virginia Tech Institutional Animal Care and Use Committee and Institutional Biosafety Committee and carried out in accordance with the National Institutes of Health Guide for the Care and Use of Laboratory Animals. Aged 7-9 weeks male C57BL/6J mice (Jackson Laboratory) were set up on a stereotaxic apparatus (David Kopf Instruments) and anesthetized by 1-3.5% isoflurane during the procedure via a nose cone. Preoperatively, buprenorphine (0.05-0.1 mg/kg) with a dose of carprofen (5 mg/kg) and Baytril (5 mg/kg) was administrated subcutaneously to prevent postsurgical pain and infections. A small incision was made behind the eyes along the midline on the bare scalp to expose the skull, and the exposed skull was scraped with a sterile tool (Fine Science Tool) to facilitate future adhesion of Metabond (C&B Metabond). A small craniotomy was made with a dental drill through which the fiber electrode was lowered using a micropositioner into the brain according to the brain atlas (coordinates relative to bregma: -2 mm anteroposterior, -1.5 mm mediolateral, and -1.9 mm dorsoventral). Then the stainless steel ground wire was soldered to a miniature screw (J.I. Morris) that was affixed to the skull by Metabond along with the exposed skull area. To further stabilize the implantation, dental cement was applied, and the implant was fully supported by the skull. Animals were

provided with a heating pad to maintain their body temperature during all procedures.

In Vivo Electrophysiology and Data Analysis. After animals recovered from the surgery, headpins were connected to a 32-channel neurophysiology system (Tucker-Davis Technologies) to perform electrophysiology recordings. The electrophysiological activities in the hippocampus were sampled with the modified electrode at ~50 kHz. The sampled activities were bandpass-filtered from 0.3 to 300 Hz and 300 to 5000 Hz to access the LFP and single-unit activities, respectively. We wrote custom scripts in MATLAB (Mathworks) to detect action potentials in the single-unit traces and to analyze the power spectral density of the LFP traces. The candidates of action potentials were detected by setting lower-bound and upper-bound voltage thresholds. These thresholds were set by visually investigating the waveforms of some action potentials and taking into account different measurements of the overall signal, such as the standard deviation, noise level, etc. Because of the neurons' inherent refractory period, the dead time was set to be 1 ms. For spike sorting, we first reduced the dimension of the candidates' voltage recordings via PCA. Then, in the principal component plane, we performed K-means clustering to cluster different numbers of candidates together. To evaluate these clusters, we computed L-ratio and isolation separation in the first 3-principal-component space. The spectrograms of the LFP recordings were created with a moving hamming window with a length of 10 s and an overlap of 7 s. The parameters can be easily manipulated in the custom script to improve the resolution or the blurriness of the spectrograms. We adopted a multitaper power spectral estimate developed by Thomson, which reduces bias in estimation by introducing pairwise orthogonal Slepian tapers to the calculation. In our script, we used seven independent Slepian tapers with a taper length of 10 s to create an estimation over a 50-s-long LFP recording. The interspike interval (ISI) histogram was computed by taking the time intervals in the same cluster and arranging the time intervals into different bins. Because of the deadtime, the ISI histogram did not contain any counts <1 ms.

Immunohistochemistry. Animals were implanted with a stainless steel probe or a surface-modified probe for 2 weeks and then anesthetized with a ketamine (20 mg/mL)/xylazine (2 mg/mL) solution and transcardially perfused with phosphate-buffered saline (PBS) (Fisher BP661-10) followed by 4% paraformaldehyde (PFA) (Electron Microscopy Sciences cat. no. 15714-S) in PBS. Upon extraction, the brain was kept in 4% PFA overnight at 4 °C and then placed into PBS containing 0.02% sodium azide (Sigma S8032). The brain was serially sectioned into 50  $\mu$ m transverse slices on a Campden Instruments 5100mz vibratome. All slices were blocked for 1 h at room temperature in a blocking solution that contained 10% goat serum (Millipore S26-100 ML) and 0.01% Triton X-100 (Sigma T9284) in PBS containing 0.02% sodium azide. After blocking, the slices were incubated with primary antibodies diluted in blocking solution without Triton X-100 overnight at room temperature. Primary antibodies used included chicken anti-GFAP (Abcam cat. no. ab4674, 1:1000), mouse anti-NeuN (Millipore cat. no. MAB377, 1:1000), and rabbit anti-Iba1 (Wako cat. no. 019-19741, 1:500). Following primary incubation, slices were washed 6 times with PBS for 10 min at room temperature with agitation. Secondary antibodies diluted in blocking solution without Triton X-100 were added at room temperature for 1 h. Secondary antibodies used included goat anti-chicken Alexa Fluor 488 (Jackson ImmunoResearch cat. no. 103-545-155, 1:500), goat anti-mouse Alexa Fluor 647 (Jackson ImmunoResearch cat. no. 115-605-062, 1:500), and goat anti-rabbit Alexa Fluor 550 (Jackson ImmunoResearch cat. no. 111-165-144, 1:500). Slices were then washed 6 times with PBS for 10 min at room temperature with agitation. Slices were mounted on glass slides with VECTASHIELD Antifade Mounting Medium with DAPI (Vector Laboratories cat. no. H-1200). Optical sections were acquired using a Nikon A1 laser scanning microscope using a Plan Apo 20X/N.A.0.75 air objective. Quantification of the volumetric data was performed using NIS-Elements (Nikon Instruments, Inc.). Neuron and microglia densities were calculated by counting NeuN and IBA1-labeled cell bodies, respectively, using spot detection. Volumetric analysis of GFAP-labeled cells was performed by creating 3D reconstructions of the optical sections using the Threshold 3D tool and quantified using 3D volumetric measurement.

#### ASSOCIATED CONTENT

# **Supporting Information**

The Supporting Information is available free of charge at https://pubs.acs.org/doi/10.1021/acsami.0c19187.

Experimental materials and methods, power spectral densities of the recording results from surface-modified and unmodified electrodes, and IHC analysis of the surface-modified and stainless steel wire (PDF)

#### AUTHOR INFORMATION

## **Corresponding Authors**

Wei Zhou — Bradley Department of Electrical and Computer Engineering, Virginia Tech, Blacksburg, Virginia 24060, United States; orcid.org/0000-0002-5257-3885; Email: wzh@vt.edu

Xiaoting Jia — Bradley Department of Electrical and Computer Engineering, Virginia Tech, Blacksburg, Virginia 24060, United States; orcid.org/0000-0003-4890-6103; Email: xjia@vt.edu

#### **Authors**

Shan Jiang — Bradley Department of Electrical and Computer Engineering, Virginia Tech, Blacksburg, Virginia 24060, United States; © orcid.org/0000-0002-1567-2745

Junyeob Song — Bradley Department of Electrical and Computer Engineering, Virginia Tech, Blacksburg, Virginia 24060, United States; © orcid.org/0000-0001-6369-823X

Yujing Zhang – Bradley Department of Electrical and Computer Engineering, Virginia Tech, Blacksburg, Virginia 24060, United States

Meitong Nie – Bradley Department of Electrical and Computer Engineering, Virginia Tech, Blacksburg, Virginia 24060, United States

Jongwoon Kim — Bradley Department of Electrical and Computer Engineering, Virginia Tech, Blacksburg, Virginia 24060, United States

Ana Lopez Marcano – Bradley Department of Electrical and Computer Engineering, Virginia Tech, Blacksburg, Virginia 24060, United States

Kelly Kadlec – Bradley Department of Electrical and Computer Engineering, Virginia Tech, Blacksburg, Virginia 24060, United States

William A. Mills, III – Translational Biology, Medicine, and Health and School of Neuroscience, Virginia Tech, Roanoke, Virginia 24016, United States

Xiaodong Yan — Ming Hsieh Department of Electrical and Computer Engineering, University of Southern California, Los Angeles, California 90089, United States

Hefei Liu — Ming Hsieh Department of Electrical and Computer Engineering, University of Southern California, Los Angeles, California 90089, United States; ⊙ orcid.org/ 0000-0001-6533-7112

Rong Tong — Department of Chemical Engineering, Virginia Tech, Blacksburg, Virginia 24061, United States;
orcid.org/0000-0002-2034-9272

Han Wang − Fralin Biomedical Research Institute, Roanoke, Virginia 24016, United States; orcid.org/0000-0001-5121-3362

Ian F. Kimbrough – School of Neuroscience, Virginia Tech, Blacksburg, Virginia 24061, United States

Harald Sontheimer — Translational Biology, Medicine, and Health and School of Neuroscience, Virginia Tech, Roanoke, Virginia 24016, United States; Fralin Biomedical Research Institute, Roanoke, Virginia 24016, United States

Complete contact information is available at: https://pubs.acs.org/10.1021/acsami.0c19187

## **Author Contributions**

<sup>∇</sup>S.J., J.S., Y.Z., and M.N. contributed equally to this work. **Author Contributions** 

S.J., J.S., A.L.M., K.K., X.J., and W.Z. designed the study. Y.Z. fabricated the multifunctional fibers. J.S. fabricated the nanohole array mask. S.J., Y.Z., A.L.M., and K.K. prepared the fiber bundle. J.S., A.L.M., M.N., X.Y., H.L., and H.W. performed e-beam evaporation. J.S., Y.Z., M.N., and A.L.M. measured SERS and RI. S.J. and R.T. obtained the impedance spectra. S.J. performed in vivo implantation surgeries and collected electrophysiological data. J.K. wrote the MATLAB script and analyzed recording data. W.A.M., S.J., I.F.K., and H.S. performed immunohistochemistry. All the authors contributed to the writing of the manuscript.

#### Notes

The authors declare no competing financial interest.

#### ACKNOWLEDGMENTS

X.J. gratefully acknowledges funding support from National Science Foundation (ECCS-1847436). W.Z. gratefully acknowledges funding support from the Air Force Office of Scientific Research (AFOSR) Young Investigator Award FA9550-18-1-0328 and National Institute of Standards and Technology (NIST) Grants 70NANB18H201 and 70NANB19H163. H.S. gratefully acknowledges funding support from U.S. National Institutes of Health (RO1-NS036692, RO1-NS082851, and RO1-NS052634). X.Y., H.L and H.W. would like to acknowledge the support from Army Research Office (Grant no. W911NF1910111) and National Science Foundation (Grant no. ECCS-1653870).

# ABBREVIATIONS

FSCV, fast-scan cyclic voltammetry; SERS, surface-enhanced Raman spectroscopy; RI, refractive index; CPE, conductive polyethylene; SEM, scanning electron microscope; FIB, focused ion beam; FDTD, finite-difference time domain; BZT, benzenethiol; ESI, electrochemical impedance spectrum; CNF, carbon nanofiber; PBS, phosphate-buffered saline; PCA, principal component analysis; LFP, local field potential; GFAP, glial fibrillary acidic protein; Iba1, ionized calcium-binding adaptor molecule 1

#### REFERENCES

- (1) Shen, Y.; Zhou, J.; Liu, T.; Tao, Y.; Jiang, R.; Liu, M.; Xiao, G.; Zhu, J.; Zhou, Z. K.; Wang, X.; Jin, C.; Wang, J. Plasmonic Gold Mushroom Arrays with Refractive Index Sensing Figures of Merit Approaching the Theoretical Limit. *Nat. Commun.* 2013, 4, 2381.
- (2) Špačková, B.; Wrobel, P.; Bocková, M.; Homola, J. Optical Biosensors Based on Plasmonic Nanostructures: A Review. *Proc. IEEE* **2016**, *104* (12), 2380–2408.
- (3) Brolo, A. G. Plasmonics for Future Biosensors. *Nat. Photonics* **2012**, *6* (11), 709–713.
- (4) Sun, F.; Hung, H. C.; Sinclair, A.; Zhang, P.; Bai, T.; Galvan, D. D.; Jain, P.; Li, B.; Jiang, S.; Yu, Q. Hierarchical Zwitterionic

- Modification of a SERS Substrate Enables Real-time Drug Monitoring in Blood Plasma. *Nat. Commun.* **2016**, *7*, 13437.
- (5) Zong, C.; Xu, M.; Xu, L. J.; Wei, T.; Ma, X.; Zheng, X. S.; Hu, R.; Ren, B. Surface-Enhanced Raman Spectroscopy for Bioanalysis: Reliability and Challenges. *Chem. Rev.* **2018**, *118* (10), 4946–4980.
- (6) Hering, K.; Cialla, D.; Ackermann, K.; Dorfer, T.; Moller, R.; Schneidewind, H.; Mattheis, R.; Fritzsche, W.; Rosch, P.; Popp, J. SERS: A Versatile Tool in Chemical and Biochemical Diagnostics. *Anal. Bioanal. Chem.* **2008**, *390* (1), 113–124.
- (7) Smythe, E. J.; Dickey, M. D.; Whitesides, G. M.; Capasso, F. A Technique to Transfer Metallic Nanoscale Patterns to Small and Nonplanar Surfaces. *ACS Nano* **2009**, *3* (1), 59–65.
- (8) Zhang, S. Y.; Tang, S. J.; Feng, S. F.; Xiao, Y. F.; Cui, W. Y.; Wang, X. K.; Sun, W. F.; Ye, J. S.; Han, P.; Zhang, X. P.; Zhang, Y. High-Q Polymer Microcavities Integrated on a Multicore Fiber Facet for Vapor Sensing. *Adv. Opt. Mater.* **2019**, 7 (20), 1900602.
- (9) Wang, Q.; Wang, L. Lab-on-fiber: Plasmonic Nano-arrays for Sensing. *Nanoscale* **2020**, *12* (14), 7485–7499.
- (10) Vaiano, P.; Carotenuto, B.; Pisco, M.; Ricciardi, A.; Quero, G.; Consales, M.; Crescitelli, A.; Esposito, E.; Cusano, A. Lab on Fiber Technology for biological sensing applications. *Laser Photonics Rev.* **2016**, *10* (6), 922–961.
- (11) Kostovski, G.; Stoddart, P. R.; Mitchell, A. The Optical Fiber Tip: An Inherently Light-Coupled Microscopic Platform for Microand Nanotechnologies. *Adv. Mater.* **2014**, *26* (23), 3798–3820.
- (12) Ricciardi, A.; Crescitelli, A.; Vaiano, P.; Quero, G.; Consales, M.; Pisco, M.; Esposito, E.; Cusano, A. Lab-on-fiber Technology: A New Vision for Chemical and Biological Sensing. *Analyst* **2015**, *140* (24), 8068–8079.
- (13) Liu, Y.; Guang, J.; Liu, C.; Bi, S.; Liu, Q.; Li, P.; Zhang, N.; Chen, S.; Yuan, H.; Zhou, D.; Peng, W. Simple and Low-Cost Plasmonic Fiber-Optic Probe as SERS and Biosensing Platform. *Adv. Opt. Mater.* **2019**, *7* (19), 1900337.
- (14) Lipomi, D. J.; Martinez, R. V.; Kats, M. A.; Kang, S. H.; Kim, P.; Aizenberg, J.; Capasso, F.; Whitesides, G. M. Patterning the Tips of Optical Fibers with Metallic Nanostructures Using Nanoskiving. *Nano Lett.* **2011**, *11* (2), 632–636.
- (15) Consales, M.; Ricciardi, A.; Crescitelli, A.; Esposito, E.; Cutolo, A.; Cusano, A. Lab-on-fiber technology: Toward Multifunctional Optical Nanoprobes. *ACS Nano* **2012**, *6* (4), 3163–70.
- (16) Ricciardi, A.; Consales, M.; Quero, G.; Crescitelli, A.; Esposito, E.; Cusano, A. Versatile Optical Fiber Nanoprobes: From Plasmonic Biosensors to Polarization-Sensitive Devices. *ACS Photonics* **2014**, *1* (1), 69–78.
- (17) Pisco, M.; Galeotti, F.; Quero, G.; Iadicicco, A.; Giordano, M.; Cusano, A. Miniaturized Sensing Probes Based on Metallic Dielectric Crystals Self-Assembled on Optical Fiber Tips. *ACS Photonics* **2014**, *1* (10), 917–927.
- (18) Nimbalkar, S.; Castagnola, E.; Balasubramani, A.; Scarpellini, A.; Samejima, S.; Khorasani, A.; Boissenin, A.; Thongpang, S.; Moritz, C.; Kassegne, S. Ultra-Capacitive Carbon Neural Probe Allows Simultaneous Long-Term Electrical Stimulations and High-Resolution Neurotransmitter Detection. *Sci. Rep.* **2018**, 8 (1), 6958.
- (19) Jun, J. J.; Steinmetz, N. A.; Siegle, J. H.; Denman, D. J.; Bauza, M.; Barbarits, B.; Lee, A. K.; Anastassiou, C. A.; Andrei, A.; Aydin, C.; Barbic, M.; Blanche, T. J.; Bonin, V.; Couto, J.; Dutta, B.; Gratiy, S. L.; Gutnisky, D. A.; Hausser, M.; Karsh, B.; Ledochowitsch, P.; Lopez, C. M.; Mitelut, C.; Musa, S.; Okun, M.; Pachitariu, M.; Putzeys, J.; Rich, P. D.; Rossant, C.; Sun, W. L.; Svoboda, K.; Carandini, M.; Harris, K. D.; Koch, C.; O'Keefe, J.; Harris, T. D. Fully Integrated Silicon Probes for High-density Recording of Neural Activity. *Nature* **2017**, *551* (7679), 232–236.
- (20) Seidl, K.; Herwik, S.; Torfs, T.; Neves, H. P.; Paul, O.; Ruther, P. CMOS-Based High-Density Silicon Microprobe Arrays for Electronic Depth Control in Intracortical Neural Recording. *J. Microelectromech. Syst.* **2011**, 20 (6), 1439–1448.
- (21) Seidl, K.; Spieth, S.; Herwik, S.; Steigert, J.; Zengerle, R.; Paul, O.; Ruther, P. In-plane Silicon Probes for Simultaneous Neural

- Recording and Drug Delivery. J. Micromech. Microeng. 2010, 20 (10), 105006.
- (22) Wu, F.; Stark, E.; Ku, P. C.; Wise, K. D.; Buzsaki, G.; Yoon, E. Monolithically Integrated muLEDs on Silicon Neural Probes for High-Resolution Optogenetic Studies in Behaving Animals. *Neuron* **2015**, 88 (6), 1136–1148.
- (23) Park, S.; Guo, Y. Y.; Jia, X. T.; Choe, H. K.; Grena, B.; Kang, J.; Park, J.; Lu, C.; Canales, A.; Chen, R.; Yim, Y. S.; Choi, G. B.; Fink, Y.; Anikeeva, P. One-step optogenetics with multifunctional flexible polymer fibers. *Nat. Neurosci.* **2017**, 20 (4), 612.
- (24) Guo, Y. Y.; Jiang, S.; Grena, B. J. B.; Kimbrough, I. F.; Thompson, E. G.; Fink, Y.; Sontheimer, H.; Yoshinobu, T.; Jia, X. T. Polymer Composite with Carbon Nanofibers Aligned during Thermal Drawing as a Microelectrode for Chronic Neural Interfaces. *ACS Nano* 2017, 11 (7), 6574–6585.
- (25) Canales, A.; Jia, X. T.; Froriep, U. P.; Koppes, R. A.; Tringides, C. M.; Selvidge, J.; Lu, C.; Hou, C.; Wei, L.; Fink, Y.; Anikeeva, P. Multifunctional Fibers for Simultaneous Optical, Electrical and Chemical Interrogation of Neural Circuits in Vivo. *Nat. Biotechnol.* **2015**, 33 (3), 277.
- (26) Yu, L.; Parker, S.; Xuan, H.; Zhang, Y.; Jiang, S.; Tousi, M.; Manteghi, M.; Wang, A.; Jia, X. Flexible Multi-Material Fibers for Distributed Pressure and Temperature Sensing. *Adv. Funct. Mater.* **2020**, *30* (9), 1908915.
- (27) Haring, A. P.; Jiang, S.; Barron, C.; Thompson, E. G.; Sontheimer, H.; He, J.-Q.; Jia, X.; Johnson, B. N. 3D Bioprinting Using Hollow Multifunctional Fiber Impedimetric Sensors. *Biofabrication* **2020**, *12*, 035026.
- (28) Ali Safiabadi Tali, S.; Zhou, W. In *Conductive Gap-Plasmon Nanocavity*; Frontiers in Optics/Laser Science, 2018/09/16; Optical Society of America: Washington, DC, 2018; p JTu2A.58.
- (29) Song, J.; Cheng, W. F.; Nie, M. T.; He, X. K.; Nam, W.; Cheng, J. T.; Zhou, W. Partial Leidenfrost Evaporation-Assisted Ultrasensitive Surface-Enhanced Raman Spectroscopy in a Janus Water Droplet on Hierarchical Plasmonic Micro-/Nanostructures. *ACS Nano* **2020**, *14* (8), 9521–9531.
- (30) Song, J.; Zhou, W. Multiresonant Composite Optical Nanoantennas by Out-of-plane Plasmonic Engineering. *Nano Lett.* **2018**, *18* (7), 4409–4416.
- (31) Song, J.; Nam, W.; Zhou, W. Scalable High-Performance Nanolaminated SERS Substrates Based on Multistack Vertically Oriented Plasmonic Nanogaps. *Adv. Mater. Technol.* **2019**, *4*, 1800689.
- (32) Ludwig, K. A.; Uram, J. D.; Yang, J. Y.; Martin, D. C.; Kipke, D. R. Chronic Neural Recordings Using Silicon Microelectrode Arrays Electrochemically Deposited with a Poly(3,4-ethylenedioxythiophene) (PEDOT) Film. *J. Neural Eng.* **2006**, *3* (1), 59–70.
- (33) Cutrone, A.; Micera, S. Implantable Neural Interfaces and Wearable Tactile Systems for Bidirectional Neuroprosthetics Systems. *Adv. Healthcare Mater.* **2019**, *8*, 1801345.
- (34) Shin, Y. M.; Kim, Y. K.; Lee, S. K.; Shin, H.; Cho, I. J.; Park, J. H. Microprobe Electrode Array with Individual Interconnects through Substrate Using Silicon Through-glass Via. *Sens. Actuators, B* **2019**, 290, 336–346
- (35) Park, H.; Takmakov, P.; Lee, H. Electrochemical Evaluations of Fractal Microelectrodes for Energy Efficient Neurostimulation. *Sci. Rep.* **2018**, *8*, 4375.
- (36) Shoar Abouzari, M. R.; Berkemeier, F.; Schmitz, G.; Wilmer, D. On the Physical Interpretation of Constant Phase Elements. *Solid State Ionics* **2009**, *180* (14–16), 922–927.
- (37) Merrill, D. R.; Bikson, M.; Jefferys, J. G. R. Electrical Stimulation of Excitable Tissue: Design of Efficacious and Safe Protocols. *J. Neurosci. Methods* **2005**, *141* (2), 171–198.
- (38) Lu, Y. C.; Liu, X.; Hattori, R.; Ren, C.; Zhang, X. W.; Komiyama, T.; Kuzum, D. Ultralow Impedance Graphene Microelectrodes with High Optical Transparency for Simultaneous Deep Two-Photon Imaging in Transgenic Mice. *Adv. Funct. Mater.* **2018**, 28 (31), 1800002.

- (39) Alexander, C. L.; Tribollet, B.; Orazem, M. E. Contribution of Surface Distributions to Constant-Phase-Element (CPE) Behavior: 1. Influence of Roughness. *Electrochim. Acta* **2015**, *173*, 416–424.
- (40) Mulder, W. H.; Sluyters, J. H.; Pajkossy, T.; Nyikos, L. Tafel Current at Fractal Electrodes Connection with Admittance Spectra. *J. Electroanal. Chem. Interfacial Electrochem.* **1990**, 285 (1–2), 103–115.